Orientation and morphology of solid-state dewetting holes

Anna Chame
Instituto de Física, Universidade Federal Fluminense, Avenida Litorânea s/n, 24210-340 Niterói, Rio de Janeiro, Brazil

Yukio Saito
Department of Physics, Keio University, 3-14-1 Hiyoshi Kohoku-ku, Yokohama, Japan

Olivier Pierre-Louis
Institut Lumière Matière, UMR5306 Université Lyon 1-CNRS, Université de Lyon, 69622 Villeurbanne, France

(Received 7 May 2020; accepted 9 September 2020; published 29 September 2020)

We report on the orientation and morphology of solid-state dewetting holes obtained from a kinetic Monte Carlo model with nearest neighbor and next nearest neighbor interactions on a cubic lattice. The morphologies found in simulations share strong similarities with those of diffusion-limited crystal growth: We find compact shapes, isotropic and anisotropic seaweed shapes, and dendritic shapes. Some of these shapes have been observed in solid-state dewetting experiments with various semi-conductors or metals on insulating substrates. The sides of the fingers can exhibit two types of zigzag instabilities with 90° or 45°. Due to fourfold symmetry, dewetting hole shapes are found to exhibit two possible orientations with fingers along the (110) or (100) directions. We find that the rotation transition from one orientation to the other can be observed in our model by varying anisotropy, temperature, or dewetting strength. The two orientations correspond, respectively, to experimental observations of dewetting for silicon and germanium on insulator and to the dewetting of metal films with different reducing gas flow rate.

DOI: 10.1103/PhysRevMaterials.4.094006

I. INTRODUCTION

Since early modeling attempts [1,2] and experimental investigations [3] in the 1990's, surface-diffusion mediated solid-state dewetting has been observed in many experiments [3–18]. These experiments have revealed that solid-state dewetting gives rise to a wide variety of morphologies, which resemble those of crystal growth, from compact or dendritic patterns, to ramified seaweedlike structures, or quasiordered arrays of fingers. This rich behavior has been used to explore nano-patterning routes [19].

Since then, most theoretical investigations have been devoted to the study of isotropic continuum models [2,20–23]. However, it has been understood from early works that crystalline anisotropy plays a major role in the genesis of this wide variety of morphologies. As a consequence, alternative strategies have been considered to model anisotropy, including continuum models [24–26] and kinetic Monte Carlo (KMC) models [27–29].

One striking result of KMC simulations [13,28–30] is the ability of a simple model with cubic symmetry and nearest neighbor (NN) interactions –described by only two dimensionless parameters– to reproduce the morphologies observed in dewetting experiments of monocrystalline Si(100) thin films on amorphous SiO_2 substrates, usually called silicon on insulator (SOI). Such results may appear surprising since the simple square lattice model with NN interactions used in these NN-KMC simulations does not account for the microscopic complexity of Si(100) surface, which exhibits a dimer raw reconstruction with alternate directions from one layer to the other. The similarity between SOI and NN-KMC morphologies suggests that a limited number of physical ingredients control the morphology of dewetting holes.

However, different dewetting hole morphologies with weaker or stronger apparent anisotropy have been reported. For example, dewetting morphologies of Ge on SiO_2 (GOI) [31] exhibit stronger apparent anisotropy than SOI. Moreover, as discussed in Ref. [31], this difference is accompanied by the transition between tip splitting and side branching instabilities of fingers, which are observed in SOI and GOI, respectively. A strikingly similar transition is well known in crystal growth, and is controlled by anisotropy [32]. In addition, the sides of GOI fingers exhibit a zigzag instability [31] that share similarities with dendrites of faceted crystals [33]. However, while 90 degrees zigzag were found in Ge dewetting holes [31], 45 degrees zigzag have been observed in experiments with metals [15]. Furthermore, isotropiclike dewetting patterns have been observed in SOI dewetting when tuning the amount of carbon contamination at the surface [34].

Beyond morphology, fingers emerging from (001) films with cubic anisotropy can exhibit two different orientations: (100) or (110). By convention, the last number in the orientation (abc) is chosen to correspond to the direction $\hat{z}$ perpendicular to the substrate. Actually, while (100) fingers were observed in SOI, previous NN-KMC simulations reported

only (110) fingers. Surprisingly, GOI dewetting exhibits (110) fingers in agreement with these NN-KMC results. A similar rotation of the finger orientation from (100) to (110) has been observed in dewetting experiments with Ni(100)/MgO when varying the flow rate of the reducing gas [15,35].

Inspired by these observations, we have investigated the role of anisotropy in solid-state dewetting using a simple KMC model, which includes not only nearest neighbor bonds, but also next nearest neighbor (NNN) bonds. This NNN-KMC model does not account for the details of material-dependent surface structure such as surface reconstructions [35], or facets such as (113) for Si and Ge, and (15,3,23) for Ge [31]. In addition, the subtle coupling between reconstructions and the size of a facet or the density of atomic steps on this facet, especially in the case of semiconductors where the unit cell of the reconstruction can be large, is discarded in our model. However, NNN-KMC reproduces many experimental observations reported in semiconductors and metallic systems within a unified picture.

Indeed, the NNN-KMC model exhibits a rotation of the fingers similar to that observed in experiments. In this model, the orientation transition can be obtained by varying the bond anisotropy, the temperature, or the dewetting strength.

Furthermore, the hole shapes emerging from NNN-KMC simulations reproduce the hole morphologies observed in SOI, GOI and metal films with fourfold symmetry. The initial shapes are compact. These shapes destabilize into dendritic shapes with high or low branching densities, with or without one of the two zigzag instabilities. In addition, close to the finger rotation transition, we find isotropic morphologies that are similar to seaweed shapes emerging from isotropic crystal growth, and that share similarities with hole shapes observed in dewetting with contamination [34].

II. MODEL

Our simulations are based on a solid-on-solid (SOS) kinetic Monte Carlo model, where the film is described by a cubic lattice on a frozen and perfectly flat substrate with (001) orientation. The hopping rate of an atom at the surface and at height z reads

$$\nu_{(n,nn)} = \nu\, \mathrm{e}^{-(n+m\zeta)J/k_BT+\delta_z E_S/k_BT}, \tag{1}$$

where n and m are, respectively, the numbers of NN and NNN before the hop. In a cubic lattice there are 6 NN and 12 NNN sites. Since in this lattice we consider only atoms at the top of a column in our SOS model that have no NN on top and always one atom below, one has $1 \leqslant n \leqslant 5$, and $0 \leqslant m \leqslant 12$. We have defined the NN bond energy J, the NNN bond energy ζJ, the Kronecker-delta symbol δ_z ($\delta_0 = 1$, and $\delta_z = 0$ for $z \neq 0$), and the thermal energy k_BT. In addition, E_S is the difference between NN bond energies in the film and NN film-substrate bonds energies [36]. In contrast to previous KMC models [27,28], we forbid diffusion on the substrate. However, no qualitative change in the results is observed when introducing substrate diffusion (see Appendix A for results of the KMC model including diffusion on the substrate).

The equilibrium shape of the NNN-KMC model includes (100), (110), and (111) facets. In the low temperature limit, the energy of the (1jk) facet reads [37]: $\epsilon_{1jk} = \sigma_{jk}^{1/2}[1 + (5 - \sigma_{jk})\zeta]J/(2a^2)$, where j and k are 0 or 1, and $\sigma_{jk} = 1 + j + k$. The facet free energies are equal to ϵ_{1jk} at low temperatures, and decrease at higher temperature. In order to compare the simulation results with different values of ζ, we define a normalized temperature τ, which is the ratio of the temperature T over the roughening temperature of the (001) facet (see Appendix B for the evaluation of the roughening temperature of the (001) facet) [38].

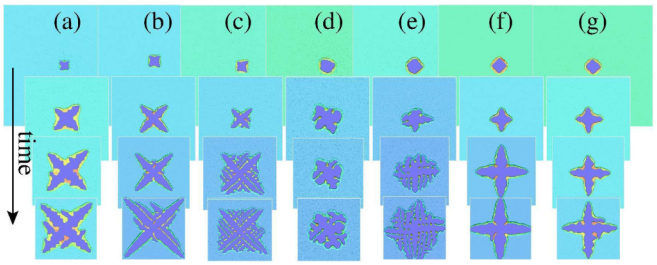

FIG. 1. Some types of dewetting holes. All images correspond to the same simulation box size 1200 × 1200. For better visualization, images have different magnification factors: Images at later times are shown with a smaller size. (a) $\zeta = 0.0$ $E_S^* = 0.7$ $\tau = 0.7$ fingers along (110), anisotropic, side-branching with 90 degrees zigzag instability; (b) $\zeta = 1.0$ $E_S^* = 1.7$ $\tau = 0.55$ fingers along (110), anisotropic, side-branching; (c) $\zeta = 0.2$ $E_S^* = 1.0$ $\tau = 0.7$ fingers along (110), anisotropic, tip-splitting; (d) $\zeta = 0.4$ $E_S^* = 0.4$ $\tau = 0.88$ isotropic, tip-splitting, seaweed; (e) $\zeta = 3.0$ $E_S^* = 0.7$ $\tau = 0.7$ fingers along (100), anisotropic, tip-splitting, seaweed; (f) $\zeta = 9.0$ $E_S^* = 4.0$ $\tau = 0.45$ fingers along (100), anisotropic, side-braching with 45 degrees zigzag instability. (g) $\zeta = 3.0$ $E_S^* = 0.7$ $\tau = 0.55$ fingers along (100), anisotropic, side-branching with 90 degrees zigzag instability.

The propensity of a system to spread or dewet, characterized here by the parameter E_S, is usually quantified in the literature by the spreading coefficient $S = \gamma_{SV} - \gamma_{SA} - \gamma_{AV}$, where γ_{SV}, γ_{SA}, and γ_{AV} are, respectively, the free energy per unit area of the bare substrate, film-substrate interface, and film surface. In the low temperature limit, free energies can be approximated by energies and $S \approx \epsilon_{SV} - \epsilon_{SA} - \epsilon_{AV}$, where ϵ_{SV}, ϵ_{SA}, and ϵ_{AV} are surface and interface energies per unit area. Using bond counting [39], we find $S \approx -E_S/a^2$. We, therefore, define the normalized quantity

$$E_S^* = -\frac{S}{2\epsilon_{100}} = \frac{E_S}{J(1+4\zeta)}. \tag{2}$$

Partial wetting is expected for $E_S^* > 0$, and the larger E_S^*, the stronger the tendency to dewet. In the isotropic limit, $S = -\gamma_{AV}(1 - \cos\theta)$, where θ is the familiar equilibrium contact angle, so that $E_S^* = (1 - \cos\theta)/2$.

As a summary, the physical behavior of the system depends on three dimensionless parameters: ζ, τ, and E_S^*.

III. RESULTS

Several types of dewetting hole morphologies emerge from our model depending on the values of the three dimensionless parameters. Some representative examples of unstable shapes are reported in Fig. 1. All simulations are performed in a square lattice of size 1200 × 1200 with initial film thickness $h = 3$. We observe that the resulting shapes closely resemble

those of dendritic growth of anisotropic crystals, with higher or lower densities of branches. We also observe a peculiar morphology in Fig. 1(d) with isotropiclike dewetting instabilities, which is similar to the so-called seaweed shapes obtained in isotropic crystal growth. Also remark that the dewetting fingers can be oriented along (110) as in Figs. 1(a), 1(b), and 1(c), but also along (100) as in Figs. 1(e), 1(f), and 1(g).

A zoom-in on the shapes of holes at early stages is presented in Fig. 2. We see clearly that the top of the rim is always facetted, as expected for temperatures $\tau < 1$. The rim height therefore grows in a layer by layer fashion, as discussed in Ref. [28].

In Fig. 3, the interior edge of the dewetting fingers is seen to undergo zigzag instabilities. There are two types of zigzag instability: 90 degrees zigzag, and 45 degrees zigzag. A 90 degrees zigzag instability where the dewetting front decomposes into segments with (100) and (010) orientations is shown in Figs. 3(a). This zigzag instability was already reported in simulations with the NN-KMC model [29], which corresponds to $\zeta = 0$. The 90 degrees zigzag instability often initiates side branching. In Ref. [29], the 90 degrees instability along (100)(010) obtained with $\zeta = 0$ was found to be an intermediate stage between the initial diffusion-limited destabilization of the edge of the dewetting front and the ultimate formation of an array of void fingers initiated at concave corners of the zigzag, which propagate into the film along the (110) direction. As shown in Fig. 3(g), we find that the 90 degrees zigzag pattern can also be observed along $(110)(1\bar{1}0)$. This instability is also often followed by the propagation of (100) void fingers emerging from concave corners. The 90 degrees zigzag instability was observed in experiments with semiconductors [31].

The 45 degrees zigzag instability, which involves (100) and (110) segments can be seen in Figs. 3(b) and 3(f). A similar instability has been reported in experiments with metallic films [15]. The relative length of segments along (100) and (110) in Figs. 3(b) and 3(f) depends on the average orientation of the dewetting front as in experiments with metal films [15]. The 45 degrees zigzag fronts are much more stable than the 90 degrees zigzag fronts, but sometimes fingers emerge from these fronts in our simulations as seen in Fig. 1(b). The 45 degrees zigzag reported in experiments on metal films were also quite stable and did not undergo fingering instabilities [15].

Figure 4 presents the dewetting hole morphologies observed in the simulations as a function of ζ and E_S^* for three normalized temperatures $\tau = 0.35$, $\tau = 0.55$, and $\tau = 0.7$.

At low temperatures $\tau = 0.35$, we observe only compact holes. As ζ is increased, the hole shapes change from a square shape with (100) edges to an octagon, and finally to a rotated square with edges along (110). Since $\tau < 1$, the (001) orientation is always below the roughening transition, and the top of the dewetting rim is facetted.

A summary of the compact shapes at $\tau = 0.35$ is reported in Fig. 5. As an important remark for Fig. 5, we do not observe any change of the compact square hole shapes (irrespective of their orientation) during the course of the simulations. In contrast, there are some cases of slow evolution for the octagonal shapes as a function of time [in the sense that the ratio of the (110) and (100) sides can change with time]. We have not been able to prove the existence of a perfectly steady asymptotic shape for octagonal shapes, due to limitations in the computational time. The shapes reported in Fig. 5, therefore, correspond to those that could be observed for the largest hole sizes, when the size of the hole is similar to that of the simulation box.

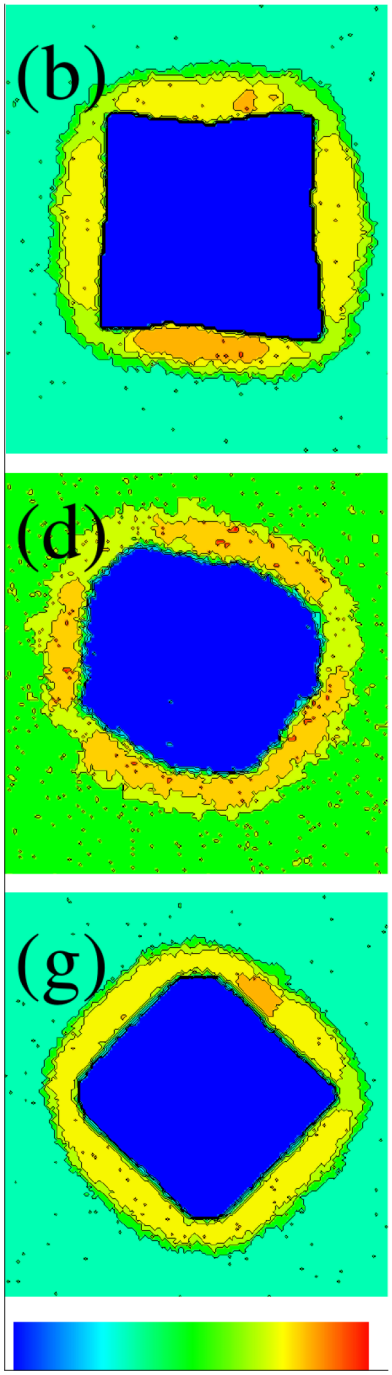

FIG. 2. Zoom-in of dewetting hole shapes at early stages from NNN-KMC. The parameters of the simulations (b), (d), and (g) correspond to those of Figs. 1(b), 1(d), and 1(g), respectively. The scale bar at the bottom of the figure represents the color scale from the substrate $z = 0$ height (dark blue) to the maximum height (red). The maximum height is $z = 8$ in (b), $z = 6$ in (d) $z = 8$ in (g). Black contour lines are shown at step edges.

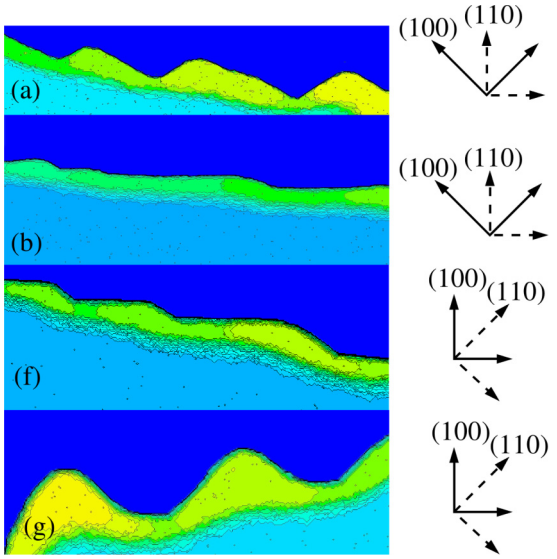

FIG. 3. Zoom-in on the zigzag instability observed in NNN-KMC. The spnapshots (a), (b), (f), and (g) are details of long times dynamics of simulations reported in Figs. 1(a), 1(b), 1(f), and 1(g), respectively. Note that the snapshots (a) and (b) are rotated by 45 degrees as compared to Fig. 1(a) 90 degrees zigzag pattern in dewetting front with (100) and (010) edge orientations. (b) 45 degrees zigzag pattern in dewetting front with (100) and (110) edge orientations. (f) 45 degrees zigzag pattern in dewetting front with (100) and (110) edge orientations. (g) 90 degrees zigzag pattern in dewetting front with (110) and ($\bar{1}$10) edge orientations. Black contour lines show atomic step edges. The color scale is the same as in Fig. 1.

Ultimately, the compact shapes are expected to be always unstable due to a corner instability similar to the Berg effect [40], or the Mullins-Sekerka instability [41]. This has already been invoked in many studies on solid-state dewetting [13,24]. By this effect, mass is expelled faster from the corners than from straight fronts. The corner instability is the first stage of the formation of fingers. This destabilization is too slow to be observed at low temperatures. However, if we increase the temperature to $\tau = 0.55$, the instability emerges before the holes reach the size of the simulation box.

Dewetting hole shapes at $\tau = 0.55$ are shown in Fig. 4(b). They show the initial stages of the instability. We find mainly holes with crosslike shapes oriented along the (100) or the (110) axis. In our simulations, void fingers form along the diagonals of the initial square holes, as expected from the corner instability. The orientation of these initial square holes corresponds roughly to those observed at lower temperatures. However, when ζ and E_S^* are both large, the sides of the initial square holes are oriented along the (100) direction at $\tau = 0.55$ while they were along (110) at lower temperatures. The orientations of dewetting holes at $\tau = 0.35$ and 0.55 are summarized in Fig. 5. Hence, the rotation of the fingers can be obtained by varying any of the three dimensionless parameter ζ, E_S^*, or τ.

Inside the crosses formed at $\tau = 0.55$ in Fig. 4(b), the interior edge of the dewetting fingers sometimes exhibits a 90 degrees zigzag instability, which often initiates side branching, and a 45 degrees zigzag instability. Such instabilities share strong similarities with experimental observations in semiconductors and metal films as discussed above.

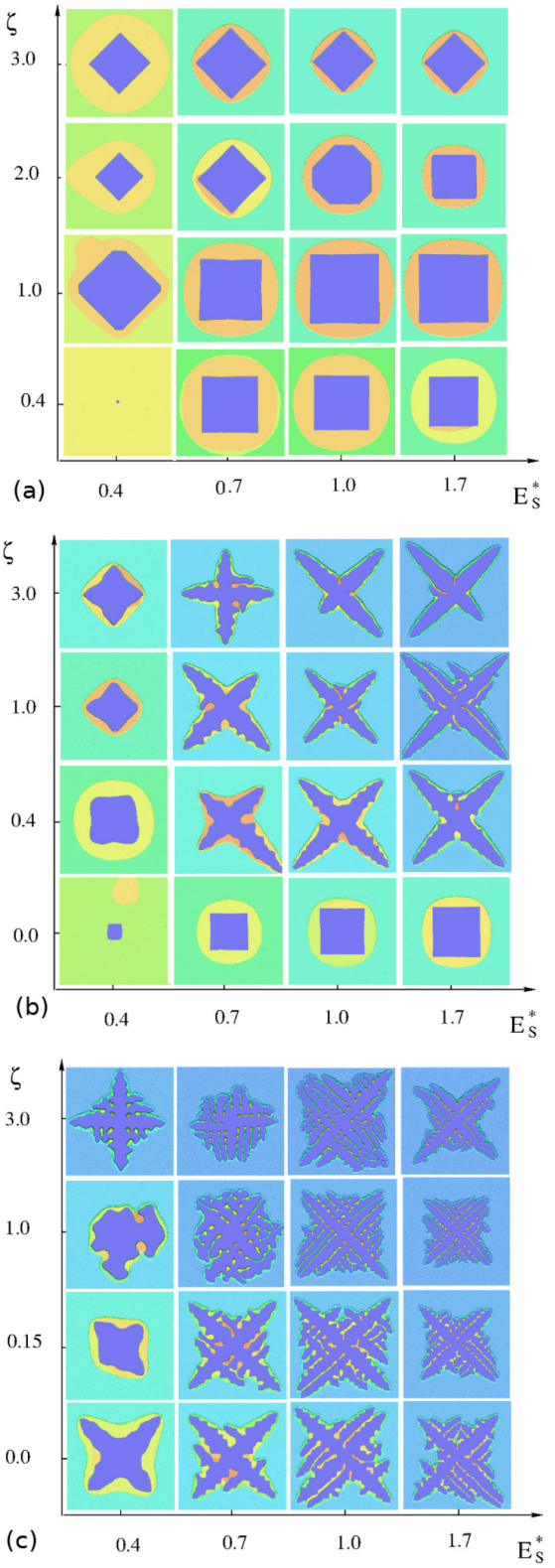

FIG. 4. Dewetting hole shapes from NNN-KMC. (a) $\tau = 0.35$, (b) $\tau = 0.55$, (c) $\tau = 0.7$. The color-scale indicates the height, from dark blue at $z = 0$ to red for the maximum height. All images are 1200×1200.

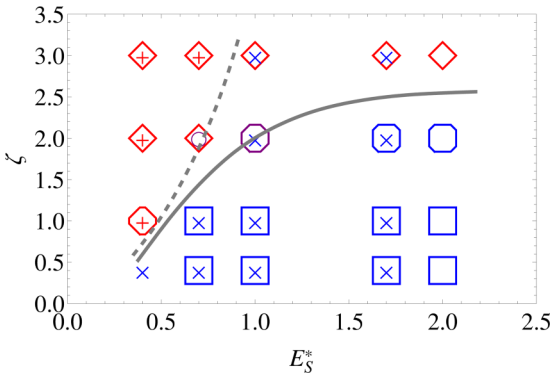

FIG. 5. Compact shapes and cross shapes. The empty symbols indicate the hole shapes observed at $\tau = 0.35$ (the relative size of the edges of the octahedrons are not quantitatively accurate). The $\times$ and $+$ represent the orientations of the initial cross [fingers along (110) or (100), respectively] in simulations at $\tau = 0.55$. The lines are guide to the eyes indicating the rotation transition : Solid $\tau = 0.35$, dashed $\tau = 0.55$.

At $\tau = 0.55$, the first branching of the fingers is often found to start at the base of the finger, along the edge of an existing finger close to the center of the cross, as observed in experiments [31]. Increasing the temperature to $\tau = 0.7$, the branching instability develops further, as seen in Fig. 4(c). We observe both branching close to the tip of the fingers, or away from the tip and the base of the fingers. These different types of branching have been observed in SOI and GOI, respectively [31]. They are refereed to as tip-splitting and side-branching [32].

Using surface free energies reported in the literature, we find that the normalized spreading coefficient and reduced temperature are similar for SOI [13] $E_S^* = 0.8$ and for GOI [31] $E_S^* = 0.7$. Since the roughening temperature of the Si(100) surface [42] is $T \approx 1473$ K, and experimental dewetting temperatures [14] are $T = 1000$ K to 1300 K, the reduced temperature for SOI is found to be between $\tau = 0.68$ and $\tau = 0.88$. Due to the lack of data on the roughening transition of Ge(100), we assume that the roughening transition is close to the melting temperature ($\approx$1211 K), leading to an approximate value of $\tau \approx 0.86$ for GOI dewetting (using temperatures from Ref. [31]). Hence, the driving force E_S^* and the reduced temperature τ seem similar for SOI and GOI. Thus, we propose that the difference between SOI and GOI dewetting can be accounted for by a difference in the structural anisotropy parameter ζ. A direct comparison with Fig. 4 for E_S^* around 0.7 suggests that describing SOI with $\zeta > 2$ and GOI with $\zeta < 1$ would lead to a rotation that is observable in the whole temperature range.

We find that $\zeta > 1.4$ corresponds to $\epsilon_{110} > \epsilon_{100} > \epsilon_{111}$ in our model. This hierarchy is in agreement with *ab initio* calculations of Si in Ref. [43]. Approximating facet free energies by facet energies, this hierarchy is also in agreement with the experimental equilibrium shape of Si by Eaglesham *et al.* [44] (however, they disagree with other experiments [45]). In agreement with these constraints, the morphologies and orientations at $\tau = 0.7$, $\zeta = 3$ and $E_S^* = 0.7$ or $E_S^* = 0.4$ shown in Fig. 4(c), indeed correspond to those observed in SOI experiments.

For the GOI case, *ab initio* simulations [43] suggest that $\epsilon_{110} > \epsilon_{111} > \epsilon_{100}$. This hierarchy is obtained for $0.4 < \zeta < 1.4$. However, the very small difference between ϵ_{111} and ϵ_{100} in Ref. [43] suggests that ζ should be around 1 or larger. As seen in Fig. 4(b), choosing ζ in this range and $\tau = 0.55$ leads to fingers along (110) in agreement with experiments. Furthermore, the fingers exhibit side-branching and undergo a 90 degrees zigzag instability, as in GOI experiments. Note that at $\tau = 0.7$, these hole morphologies are observed for lower values of ζ. Hence, we speculate that τ is closer to 0.55 than to the value $\tau \approx 0.86$ based on the melting temperature.

In the case of metal films, the increase of the reducing gas flow rate was shown to induce a rotation of compact holes from squares with sides along (100) to squares with sides along (110) for Ni(100) [15,35] and Pd(100) [46]. Close to the transition, the compact holes exhibit an octagonal shape similar to our simulation results [46]. Increasing the reducing gas flow rate decreases the amount of oxygen in the system [15]. When there is no oxygen adsorption on the surface, the (111) orientation usually exhibits a lower energy. In the presence of oxygen adsorption, (100), (110), and (111) facets reconstruct and usually exhibit similar energies (see, e.g., studies of Pt group metals [47]). In addition, cross sectional scanning electron microscopy images of the rims do not show significant change in the contact angle when changing the gas flow rate in Ni(100) films [35]. Since the (111) surface is the most stable when ζ is large, we conclude that increasing the gas flow rate is similar to increasing ζ. Hence, as shown in Fig. 5, increasing the gas flow rate is expected to lead to a rotation that is consistent with the global trend of experimental results on metal films.

A different regime is found when the anisotropy of the edge of the dewetting fronts is small. The dynamics are presented in Fig. 4(c) at $\tau = 0.7$, $E_S^* = 0.4$, and $\zeta = 1$, and in Fig. 1(d). This regime can be found close to the rotation transition, when both (100) and (110) edges exhibit similar free energies. The width of the region in which isotropic dewetting is observed increases with temperature (see, e.g., Fig. 4(c) $\zeta = 1$, isotropic dynamics is seen both for $E_S^* = 0.4$ and 0.7). One important remark is that $\tau < 1$ and we are below the roughening transition of the (100) orientation. Hence, surface tension is still globally strongly anisotropic. As seen in Fig. 2(d), a (100) facet is always present at the top of the rim.

These isotropic morphologies share similarities with those of isotropic dewetting of SOI with contamination [34].

IV. CONCLUSION

In conclusion, we have presented a simple KMC model with three parameters that is able to reproduce many experimental solid-state dewetting hole shapes for systems with cubic symmetry, and which exhibits a non-trivial rotation of the hole shape, as observed in semiconductors (SOI, GOI), and metal films experiments. Some unstable shapes observed in the simulations are presented in Fig. 1. In addition, the edges of the fingers can undergo 90 degrees and 45 degrees zigzag instabilities, as reported in GOI and metal film

dewetting experiments, respectively. At shorter times and low temperatures, compact shapes are found. The NNN-KMC model is a modeling framework that provides a unified view of the consequences of anisotropy. The NNN-KMC model therefore appears as a versatile tool for the investigation of solid-state dewetting.

Maybe one of the most promising observations of our work is that of isotropic seaweedlike shapes. Since this dewetting mode has not been observed before, this opens a challenge to find the conditions under which such shapes can be found in experiments and in simulations based on continuous models.

A wider open question is to draw a global conceptual framework that encompasses shapes observed in crystal growth, liquid-state dewetting, and solid-state dewetting. We expect some fundamental differences between these three physical systems. The first one is the local conservation of mass in liquid and solid-state dewetting, which leads, e.g., to continuum dynamical equations which are fourth-order in space. Such high-order evolution equations can give rise to oscillations in the shape beyond the dewetting rim. The growth of these oscillations can lead to the pinching of the film behind the dewetting rim, as discussed initially in Ref. [20]. The faceting of the film can prevent this pinching [28]. However, a nontrivial wetting potential such as that resulting from quantum confinement in nanometric metal films can enhance the pinching [48]. Another important difference is that in crystal growth, the anisotropy is only present at the surface of the solid, while in solid-state dewetting, anisotropy is present in the "bulk" away from the front.

However, the results of the NNN-KMC model suggest that, -at least for fourfold anisotropy, the shapes of dewetting holes are very similar to those found in crystal growth. How can different systems with such major differences (mass-conservation or not, anisotropy in the bulk or at the front) give rise to similar dynamical shapes? A possible direction of investigation for this question is to consider systems that make link between the different limits. For example, the breaking of mass conservation in solid-state dewetting due to evaporation on the substrate can lead to different dynamics with steady and constant-speed dewetting rims as found in Ref. [49]. Another direction is the investigation of liquid dewetting on anisotropic substrates, which exhibit an isotropic "bulk" behavior away from the front, but anisotropy at the front due to an anisotropic triple line. This has been studied experimentally both with microscale patterns [50,51] (for which pinning effects come to the fore), and at the nanoscale using the surface anisotropy of crystalline solid substrates [52,53]. We hope that our work will motivate further theoretical and experimental investigations in this direction.

ACKNOWLEDGMENTS

We thank P. Müller, F. Leroy, F. Cheynis, and S. Curiotto in CINAM, C.V. Thompson and his group at MIT, and J. Ye at INHA University for useful discussions. We acknowledge support from Ciência sem Fronteiras/CNPq Grant No. PVE 400578/2012-3, from the Brazilian agency CAPES (Grant No. 88887.369967/2019-00), and from ANR-12-BS04-0008 (LOTUS).

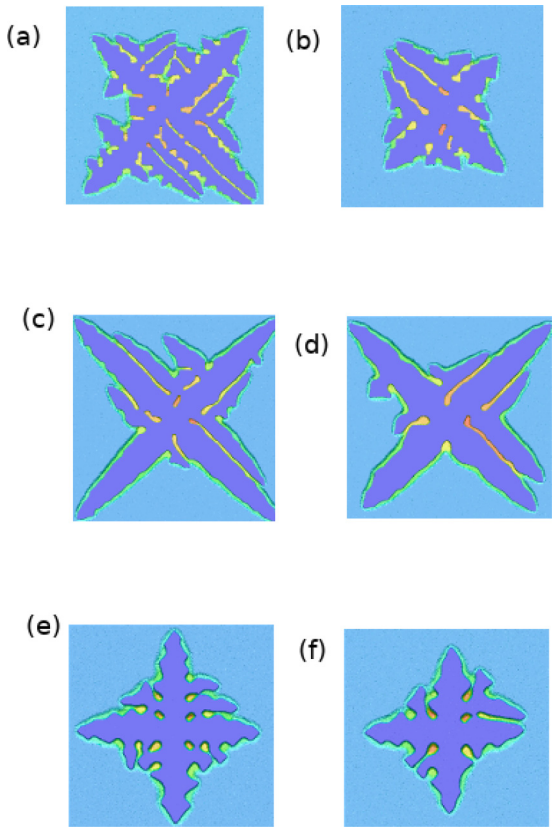

FIG. 6. Snapshots of 1200×1200 KMC simulations. Each line compares, for the same set of parameters, the image obtained considering no adatom diffusion on the substrate (left side) with the image obtained considering adatom diffusion on the substrate (right side). (a) and (b) for $\zeta = 0.0$, $E_S^* = 1.7$ and $\tau = 0.7$, (c) and (d) for $\zeta = 1.0$, $E_S^* = 1.7$ and $\tau = 0.55$, (e) and (f) for $\zeta = 3.0$, $E_S^* = 0.4$ and $\tau = 0.7$.

APPENDIX A: THE INFLUENCE OF DIFFUSION ON THE SUBSTRATE

In this work, no adatom diffusion on the substrate is considered. In Fig. 6, we compare the results obtained with and without adatom diffusion on the substrate.

We find that the dewetting rate is slightly slower, and the width of the branches is slightly larger in the presence of substrate diffusion. However, the shapes of the unstable dewetting holes are very similar.

APPENDIX B: ROUGHENING TRANSITION

The free energy of an atomic step on the (001) facet along the (100) direction can be calculated considering kinks of arbitrary height and neglecting overhangs [38]

$$\beta_{\text{step}}(T) = \frac{J}{2a}(2\zeta + 1) - T \ln\left[\frac{e^{(2\zeta-1)/(4T)}}{\sinh\left((2\zeta+1)/(4T)\right)} + 1\right] \tag{B1}$$

at the temperature T (in units with $k_B = 1$).

At the roughening transition $T = T_r$, the step-free energy vanishes: $\beta_{\text{step}} = 0$. We therefore extract T_r numerically from the equation $\beta_{\text{step}}(T_r) = 0$.

[1] R. Brandon and F. J. Bradshaw, *The Mobility of the Surface Atoms of Copper and Silver Evaporated Deposits,*Technical Report, Royal Aircraft Establishment (Farnborough, United Kingdom, 1966), p. 38.

[2] D. Srolovitz and S. Safran, Capillary instabilities in thin films: Ii kinetics, J. Appl. Phys. **60**, 255 (1986).

[3] E. Jiran and C. Thompson, Capillary instabilities in thin, continuous films, Thin Solid Films **208**, 23 (1992).

[4] K. Thürmer, E. D. Williams, and J. E. Reutt-Robey, Dewetting dynamics of ultrathin silver films on Si(111), Phys. Rev. B **68**, 155423 (2003).

[5] B. Krause, A. C. Dürr, F. Schreiber, H. Dosch, and O. H. Seeck, Thermal stability and partial dewetting of crystalline organic thin films: 3, 4, 9, 10-perylenetetracarboxylic dianhydride on Ag(111), J. Chem. Phys. **119**, 3429 (2003).

[6] B. Yang, P. Zhang, D. E. Savage, M. G. Lagally, G.-H. Lu, M. Huang, and F. Liu, Self-organization of semiconductor nanocrystals by selective surface faceting, Phys. Rev. B **72**, 235413 (2005).

[7] M. Coll, J. Gázquez, A. Pomar, T. Puig, F. Sandiumenge, and X. Obradors, Stress-induced spontaneous dewetting of heteroepitaxial Y Ba_2 Cu_3 O_7 thin films, Phys. Rev. B **73**, 075420 (2006).

[8] E. Dornel, J.-C. Barbé, F. de Crécy, G. Lacolle, and J. Eymery, Surface diffusion dewetting of thin solid films: Numerical method and application to Si/SiO_2, Phys. Rev. B **73**, 115427 (2006).

[9] Z. A. Burhanudin, R. Nuryadi, Y. Ishikawa, and M. Tabe, Transition from wire formation to island formation in thermal agglomeration of a (111)silicon -on -insulator layer, Thin Solid Films **508**, 235 (2006).

[10] K. F. McCarty, J. C. Hamilton, Y. Sato, A. Saà, R. Stumpf, J. de la Figuera, K. Thürmer, F. Jones, A. K. Schmid, A. A. Talin, and N. C. Bartelt, How metal films de-wet substrates identifying the kinetic pathways and energetic driving forces, New J. Phys. **11**, 043001 (2009).

[11] E. J. Luber, B. C. Olsen, C. Ophus, and D. Mitlin, Solid-state dewetting mechanisms of ultrathin Ni films revealed by combining in situ time resolved differential reflectometry monitoring and atomic force microscopy, Phys. Rev. B **82**, 085407 (2010).

[12] H. Galinski, T. Ryll, P. Elser, J. L. M. Rupp, A. Bieberle-Hütter, and L. J. Gauckler, Agglomeration of Pt thin films on dielectric substrates, Phys. Rev. B **82**, 235415 (2010).

[13] E. Bussmann, F. Cheynis, F. Leroy, P. Müller, and O. Pierre-Louis, Dynamics of solid thin-film dewetting in the silicon-on-insulator system, New J. Phys. **13**, 043017 (2011).

[14] F. Cheynis, E. Bussmann, F. Leroy, T. Passanante, and P. Müller, Dewetting dynamics of silicon-on-insulator thin films, Phys. Rev. B **84**, 245439 (2011).

[15] J. Ye and C. V. Thompson, Anisotropic edge retraction and hole growth during solid-state dewetting of single crystal nickel thin films, Acta Mater. **59**, 582 (2011).

[16] C. V. Thompson, Solid-state dewetting of thin films, Annu. Rev. Mater. Res. **42**, 399 (2012).

[17] F. Leroy, F. Cheynis, T. Passanante, and P. Müller, Dynamics, anisotropy, and stability of silicon-on-insulator dewetting fronts, Phys. Rev. B **85**, 195414 (2012).

[18] M. Aouassa, L. Favre, A. Ronda, H. Maaref, and I. Berbezier, The kinetics of dewetting ultra-thin Si layers from silicon dioxide, New J. Phys. **14**, 063038 (2012).

[19] J. Ye and C. V. Thompson, Templated solid-state dewetting to controllably produce complex patterns, Adv. Mater. **23**, 1567 (2011).

[20] H. Wong, P. Voorhees, M. Miksis, and S. Davis, Periodic mass shedding of a retracting solid film step, Acta Mater. **48**, 1719 (2000).

[21] W. Kan and H. Wong, Fingering instability of a retracting solid film edge, J. Appl. Phys. **97**, 043515 (2005).

[22] M. Naffouti, R. Backofen, M. Salvalaglio, T. Bottein, M. Lodari, A. Voigt, T. David, A. Benkouider, I. Fraj, L. Favre, A. Ronda, I. Berbezier, D. Grosso, M. Abbarchi, and M. Bollani, Complex dewetting scenarios of ultrathin silicon films for large-scale nanoarchitectures, Sci. Adv. **3**, eaao1472 (2017).

[23] A. K. Tripathi and O. Pierre-Louis, Triple-line kinetics for solid films, Phys. Rev. E **97**, 022801 (2018).

[24] R. V. Zucker, G. H. Kim, J. Ye, W. C. Carter, and C. V. Thompson, The mechanism of corner instabilities in single-crystal thin films during dewetting, J. Appl. Phys. **119**, 125306 (2016).

[25] W. Jiang, Y. Wang, Q. Zhao, D. J. Srolovitz, and W. Bao, Solid -state dewetting and island morphologies in strongly anisotropic materials, Scr. Mater. **115**, 123 (2016).

[26] M. Salvalaglio, R. Backofen, R. Bergamaschini, F. Montalenti, and A. Voigt, Faceting of equilibrium and metastable nanostructures: A phase - field model of surface diffusion tackling realistic shapes, Cryst. Growth Des. **15**, 2787 (2015).

[27] O. Pierre-Louis, A. Chame, and Y. Saito, Dewetting of a Solid Monolayer, Phys. Rev. Lett. **99**, 136101 (2007).

[28] O. Pierre-Louis, A. Chame, and Y. Saito, Dewetting of Ultrathin Solid Films, Phys. Rev. Lett. **103**, 195501 (2009).

[29] M. Dufay and O. Pierre-Louis, Anisotropy and Coarsening in the Instability of Solid Dewetting Fronts, Phys. Rev. Lett. **106**, 105506 (2011).

[30] M. Trautmann, F. Cheynis, F. Leroy, S. Curiotto, O. Pierre-Louis, and P. Müller, Dewetting of patterned solid films: Towards a predictive modeling approach, Appl. Phys. Lett. **110**, 263105 (2017).

[31] F. Leroy, F. Cheynis, T. Passanante, and P. Müller, Influence of facets on solid state dewetting mechanisms: Comparison between Ge and Si on SiO_2, Phys. Rev. B **88**, 035306 (2013).

[32] See, e.g., Y. Saito, *Statistical Physics of Crystal Growth* (World Scientific, Singapore, 1996).

[33] J. Maurer, P. Bouissou, B. Perrin, and P. Tabeling, Faceted dendrites in the growth of NH_4Br crystals, Europhys. Lett. **8**, 67 (1989).

[34] F. Leroy, L. Borowik, F. Cheynis, Y. Almadori, S. Curiotto, M. Trautmann, J. Barbé, and P. Müller, How to control solid state dewetting: A short review, Surf. Sci. Rep. **71**, 391 (2016).

[35] G. H. Kim, W. Ma, B. Yildiz, and C. V. Thompson, Effect of annealing ambient on anisotropic retraction of film edges during solid-state dewetting of thin single crystal films, J. Appl. Phys. **120**, 075306 (2016).

[36] For the sake of simplicity, we consider that the energies of the NNN bonds between the film and the substrate at the interface are the same as the NNN bond energies in the bulk of the film.

[37] O. Pierre-Louis and Y. Saito, Wetting of solid islands on parallel nano-grooves, Europhys. Lett. **86**, 46004 (2009).

[38] M. Ignacio, Theoretical study of solids nanocrystals wetting on nanopatterned substrates, Ph.D. thesis, Université Claude Bernard - Lyon I, 2014.

[39] O. Pierre-Louis, A. Chame, and M. Dufay, Atomic step motion during the dewetting of ultra-thin films, Eur. J. Phys. B **77**, 57 (2010).

[40] W. F. Berg and W. L. Bragg, Crystal growth from solutions, Proc. R. Soc. London A **164**, 79 (1938).

[41] W. W. Mullins and R. F. Sekerka, Morphological stability of a particle growing by diffusion or heat flow, J. Appl. Phys. **34**, 323 (1963).

[42] N. C. Bartelt, R. M. Tromp, and E. D. Williams, Step capillary waves and equilibrium island shapes on Si(001), Phys. Rev. Lett. **73**, 1656 (1994).

[43] A. A. Stekolnikov and F. Bechstedt, Shape of free and constrained group-iv crystallites: Influence of surface energies, Phys. Rev. B **72**, 125326 (2005).

[44] D. J. Eaglesham, A. E. White, L. C. Feldman, N. Moriya, and D. C. Jacobson, Equilibrium shape of Si, Phys. Rev. Lett. **70**, 1643 (1993).

[45] J. Bermond, J. Métois, X. Egéa, and F. Floret, The equilibrium shape of silicon, Surf. Sci. **330**, 48 (1995).

[46] J. Ye, Shape anisotropy and instability of holes formed during dewetting of single-crystal palladium and nickel films, J. Vac. Sci. Technol. A **33**, 060601 (2015).

[47] N. Seriani and F. Mittendorfer, Platinum-group and noble metals under oxidizing conditions, J. Phys.: Condens. Matter **20**, 184023 (2008).

[48] A. Chame and O. Pierre-Louis, Solid-state dewetting with a magic thickness: Electronic dewetting, Phys. Rev. B **90**, 195408 (2014).

[49] A. Chame and O. Pierre-Louis, Dewetting of solid films with substrate-mediated evaporation, Phys. Rev. E **85**, 011602 (2012).

[50] T. Cubaud and M. Fermigier, Faceted drops on heterogeneous surfaces, Europhys. Lett. **55**, 239 (2001).

[51] M. L. Blow, H. Kusumaatmaja, and J. M. Yeomans, Imbibition through an array of triangular posts, J. Phys.: Condens. Matter **21**, 464125 (2009).

[52] B. Ressel, K. C. Prince, S. Heun, and Y. Homma, Wetting of Si surfaces by AuSi liquid alloys, J. Appl. Phys. **93**, 3886 (2003).

[53] S. Curiotto, F. Leroy, F. Cheynis, and P. Müller, Self-propelled motion of AuSi droplets on Si(111) mediated by monoatomic step dissolution, Surf. Sci. **632**, 1 (2015).